Line-graph-lattice crystal structures of stoichiometric materials

Christie S. Chiu
Department of Electrical Engineering, Princeton University, Princeton, New Jersey 08544, USA
and Princeton Center for Complex Materials, Princeton University, Princeton, New Jersey 08540, USA

Annette N. Carroll
Department of Physics, Princeton University, Princeton, New Jersey 08544, USA

Nicolas Regnault
Department of Physics, Princeton University, Princeton, New Jersey 08544, USA

Andrew A. Houck
Department of Electrical Engineering, Princeton University, Princeton, New Jersey 08544, USA

(Received 25 October 2021; accepted 24 January 2022; published 22 April 2022)

The origin of many quantum-material phenomena is intimately related to the presence of flat electronic bands. In quantum simulation, such bands have been realized through line-graph lattices, a class of lattices known to exhibit flat bands. Based on that work, we conduct a high-throughput screening for line-graph lattices among the crystalline structures of the Materials Flatband Database and report on new candidates for line-graph materials and lattice models. In particular, we find materials with line-graph-lattice structures beyond the two most commonly known examples, the kagome and pyrochlore lattices. We also identify materials that may exhibit flat topological bands. Finally, we examine the various line-graph lattices detected and highlight those with gapped flat bands and those most frequently represented among this set of materials. With the identification of real stoichiometric materials and theoretical lattice geometries, the results of this work may inform future studies of flat-band many-body physics in both condensed matter experiment and theory.

DOI: 10.1103/PhysRevResearch.4.023063

I. INTRODUCTION

Within a dispersionless band of a crystalline solid, electrons have diverging effective mass and localized wave functions can remain localized, notably in the absence of disorder. The inclusion of Coulomb repulsion then gives rise to strongly interacting many-body systems, which have been predicted to exhibit phenomena ranging from ferromagnetism [1–4] and flat-band many-body localization [5–10], to unconventional superconductivity [11–14] and zero-magnetic-field fractional quantum Hall states [15–18]. Experimental work, too, has targeted flat-band physics, for example through quantum simulation on various platforms such as photonics [19–22], quantum circuits [23,24], and ultracold atoms [25,26], as well as on materials such as magic-angle twisted bilayer graphene and twisted bilayer transition-metal dichalcogenides [27–31].

Certain families of lattices are known to host flat bands. For example, bipartite lattices have flat bands at the center of their spectra, with band degeneracy equal to the difference in number of sites per unit cell in each sublattice; the Lieb lattice is a well-known example [32]. Additionally, mathematical generators of flat-band lattices have been proposed [33,34]. Specific lattices have also been identified to host flat bands, including the kagome [35] and pyrochlore lattices [36], see Fig. 1(a). These are both examples of line-graph lattices, though their flat bands are not gapped [1,2].

Line graphs are graphs (a set of vertices connected by edges) that reflect the adjacency between edges of another graph, which we term the root graph, see Fig. 1(b). More specifically, every edge in the root graph is represented by a vertex in its line graph, and edges in the line graph connect vertices arising from incident edges in the root graph. The adjacency matrix of a line graph can be shown to have -2 as its lowest eigenvalue [37]. Through the addition of discrete translation invariance, (finite-size) line graphs can be extended to line-graph lattices. Correspondingly, for dimensions $D > 1$ the associated tight-binding Hamiltonian with amplitude-1 hopping exhibits one or more exactly flat band or bands at the bottom of the spectrum, with eigenvalue -2 [38], see Appendix A for details.

Line-graph lattices have emerged as a means for generating flat bands within the field of quantum simulation with superconducting circuits. In particular, lattices of microwave cavities have been constructed as a path towards simulating condensed matter systems [23,39]. In such lattices, each cavity acts as a lattice site for photons. As a result, a circuit layout with cavities on every edge and capacitive coupling between cavities at each vertex simulates the corresponding line graph.

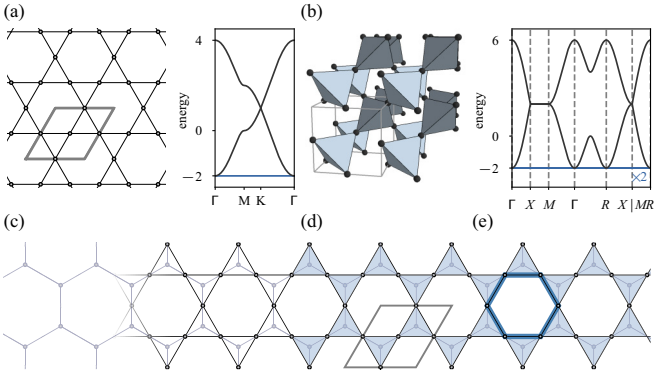

FIG. 1. (a) The kagome lattice and (b) a pyrochlore-like lattice, and their band energies through high-symmetry points of their respective Brillouin zones. The kagome lattice is the line graph of the honeycomb lattice, and the pyrochlore lattice is the line graph of the diamond lattice. Under the tight-binding model with *s*-orbital-like hopping of amplitude 1, these lattices exhibit exactly flat bands at eigenvalue −2. Lattice sites are denoted with circles, and hopping between them shown by lines. Unit cells are outlined in gray. For pyrochlore, tetrahedra are colored to aid visibility of the lattice structure. (c) A honeycomb lattice (left) with the kagome overlaid (right), highlighting the line-graph construction connecting the two. (d) The Krausz-(2, 1) partition for the kagome lattice. Here cliques of size 3, which look like triangles, are highlighted in blue. Because each vertex is part of at most two of these cliques, and each edge is part of exactly one clique, this is indeed a valid Krausz partition. The number and arrangement of cliques per unit cell (outlined in gray) characterizes the lattice, see main text. We also note that the tetrahedra coloring of (b) represents a Krausz partition for the pyrochlore lattice. (e) Line-graph lattices in two dimensions can be further characterized by considering faces of the lattice, here outlined in blue. See main text for details.

Stemming from these ideas, the topology of line-graph-lattice flat bands has been examined; line-graph lattices and line-graph lattices with select perturbations have been theoretically shown to have exactly flat or nearly flat fragile topological bands [40,41].

More generally, the identification and characterization of flat-band lattice models is integral to theoretical and experimental work [42]. For example, the kagome lattice is a rich theoretical playground for studying magnetism and resonating valence bond states [43,44]. More recently, it has inspired materials design to experimentally realize Dirac cones and flat bands [45,46]. Similarly, the pyrochlore lattice has also been the focus of theoretical simulation and first-principles calculations [47]. Much work has been done to identify flat-band materials and classify those with bipartite structure—including split-graph lattices and the Lieb lattice—or with kagome or pyrochlore sublattices [48]. However, prior to this work, it was not known what other crystal structures, if any, are line-graph lattices.

Here we develop and execute a high-throughput screening for crystalline structures that are line-graph lattices. The materials are from the Materials Flatband Database [48,49]. This database identifies flat-band materials from the Topological Quantum Chemistry web site [50,51], which contains most stoichiometric structures from the Inorganic Crystal Structure Database (ICSD). Of the 55206 ICSDs in the Materials Flatband Database, we find 4409 hosting line-graph lattice crystalline structures, 2970 of which are not kagome or pyrochlore structures. Our results are publicly available on the Materials Flatband Database. Furthermore, we find over 388 unique line-graph lattices, verified to be consistent with line graphs by computing the tight-binding model band spectra. Because line-graph lattices exhibit flat bands due to geometric frustration rather than fine-tuned parameters, these materials and their underlying lattices are particularly promising for materials engineering and design, first-principles theoretical study, and quantum simulation.

II. METHOD

Our algorithm to determine whether a given lattice is a line graph relies upon one key insight: line-graph lattices are composed of fully connected subgraphs, where each bond is part of exactly one subgraph and each site can be a part of at most two subgraphs. Within graph theory, these fully connected subgraphs are known as cliques. Such a clique partitioning is called a Krausz-(2, 1) partition [52], which we will refer to as a Krausz partition for simplicity. If a Krausz partition exists, the resulting graph is a line graph; otherwise, it is not. The partitions for the kagome and pyrochlore lattices are shown in Figs. 1(d) and 1(b), respectively. We note that this is a purely geometric method of identifying line-graph lattices, based solely on the connectivity of sites. It does not depend on the space symmetry group of the material or occupation of particular high-symmetry points in the lattice (maximal Wyckoff positions).

With this particular consideration in mind, our search proceeds over all Material Flatband Database ICSD entries as follows, see Fig. 2. First, we determine the lattice structure, given by the connectivity of atomic sites and its dimension. Following Ref. [48], we assume that the hopping between any two atoms depends on their spatial separation and place a cutoff for long bond lengths. The search is iterated on various cutoff parameters, detailed in Appendix B. We search over the resulting three-dimensional (3D) structures to extract lattice geometries with flat bands over the entire 3D Brillouin zone. In addition, we search over 2D structures on the various Miller planes to identify lattices with flat bands along a 2D plane of the Brillouin zone.

Second, we determine whether each structure is a line-graph lattice. This begins by checking the effective dimensionality of the structure, to analyze only those which are 2D, quasi-2D, or 3D. Next, we check whether the number of edges (bonds) is below the upper limit for a line-graph lattice, given its number of vertices (sites). At this point, note that any algorithm to search for a Krausz partition is likely better suited for finite-sized graphs. To reduce such a graph without affecting whether it is a line graph, we isolate all of the edges of a single unit cell and their adjacent vertices, such that this graph can be translated by the lattice vectors to construct the entire lattice. Crucially, while no two edges of this reduced graph are translationally invariant, this is not the case for the vertices. Upon rearranging these edges and vertices under only lattice vector translations, we create finite-sized

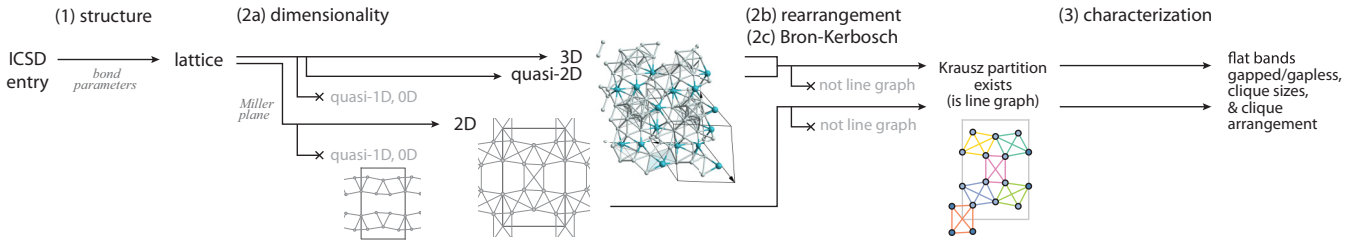

FIG. 2. Workflow illustration of line-graph-lattice screening, following the discussion in the main text. In (1), lattice structures are determined from an ICSD and set of bond parameters. In (2), we determine whether the structure is a line-graph lattice via (a) its dimensionality, (b) rearrangement to a finite-sized graph, and (c) the Bron-Kerbosch algorithm. In (3), we categorize and filter any extracted line-graph lattices. The example lattices shown are from ICSD 674920, where the two-dimensional (2D) and quasi-1D lattices are from Miller plane $(1\bar{1}1)$. In this example, only the 2D lattice structure is a line graph.

graphs, which will be line graphs if and only if the original lattice is a line-graph lattice. In the interest of computational efficiency, at this point we ignore lattices that are too complex, however, we estimate the effects of this to be small, see Appendix B for details. The cliques can then be extracted via the Bron-Kerbosh algorithm [53], from which the presence or absence of a Krausz partition can be determined. We can test the success of our algorithm by calculating the tight-binding spectra of our detected line-graph lattices and confirming the presence of exactly flat bands at -2 across their respective 3D or 2D Brillouin zones. Additional details of our algorithm can be found in Appendix B.

Finally, we filter the line-graph lattices themselves. This characterization allows us to identify the prevalence of the kagome and pyrochlore lattices among our extracted materials. It also allows us to identify other common line-graph lattices that may be of interest for theoretical study. The most coarse-grained criteria is the dimensionality of the lattice. Next, we tabulate the sizes of the clique(s) adjacent to each vertex in the unit cell and count the frequency of each clique-size singlet or pair. Lattices, which only differ by integer multiples of these frequencies, are grouped together. This accounts for lattices whose unit cells are different sizes but otherwise equivalent, for example, lattices whose unit cells are comprised of two copies of the unit cell of another lattice.

As examples, the characterizations for the pyrochlore and kagome lattices can be seen from Figs. 1(b) and 1(d). The depicted pyrochlore unit cell consists of two size-4 cliques, with light and dark coloring. There are four vertices per unit cell, and each is shared by two size-4 cliques. The kagome characterization is similarly simple: the unit cell consists of two size-3 cliques, and each of the three vertices per unit cell is shared by two size-4 cliques.

In two dimensions, additional characterizations are possible. In particular, if edge crossings within a clique are permitted (but not across multiple cliques), then the graph can be embedded on a torus. The concept of faces of this graph, neglecting the regions bounded by cliques, is then well defined: they are regions bounded by edges and vertices that contain no other edges or vertices. For the kagome lattice, as seen in Fig. 1(e), these faces correspond to the nonshaded (nonclique) regions. They are all hexagons, bounded by six edges and six vertices, as outlined in blue.

As a result, we can determine the size and number of faces per unit cell, the ordered list of clique sizes adjacent to each face, and the two face sizes adjacent to each vertex. The kagome lattice contains one hexagon (size-6 face) per unit cell with six size-3 cliques adjacent to it, and two size-6 faces are adjacent to each vertex. As before, lattices that only differ by integer multiples of these frequencies are grouped together. These attributes fully define the graph, such that the graphs of each group are isomorphic to one another. By contrast, these characterizations are not possible in three dimensions. Our groups of quasi-2D and 3D line-graph lattices may then in fact consist of multiple similar but nonisomorphic lattices, so our cited number of unique line-graph lattices is a lower bound.

III. RESULTS

One may not expect to find many crystal structures that are line-graph lattices. As these lattices are fully comprised of cliques, they contain clusters of atomic sites with all-to-all tunneling of equal amplitude—a feature that seems relatively uncommon. Indeed, under criteria identifying different features of the kagome and pyrochlore lattices from those examined here, related work has identified just over 11% and 3% of Flatband Materials Database entries hosting kagome and pyrochlore sublattices, respectively [48].

The summary of our results is in Table I. Our identified line-graph materials and lattices can be found in the Materials Flatband Database and tables of the line-graph materials are included as Supplemental Material [54]. Among the 55206 ICSD entries screened, we find a select set of unique ICSDs with line-graph crystal structures. Of these, the line graphs are 3D in 729 ICSDs, quasi-2D in 131 ICSDs, and lie on a 2D Miller plane in 3761 ICSDs. Among 3D lattices, 443 ICSDs are pyrochlorelike. Here, this means that the lattice structure is comprised entirely of size-4 and size-5 cliques where the cliques of size 4 (5) correspond to (center-occupied) tetrahedra, each with all-to-all hopping between the four (five) sites. Their flat bands are also ungapped. We note that this is an upper bound on the ICSDs, which have a pyrochlore lattice structure, as there may exist lattices that fit the above criteria but are not isomorphic to the pyrochlore lattice, for example the one in Fig. 3(b). There may also be ICSDs that, for different bond cutoffs, create distinct line-graph lattices. Within these, both pyrochlorelike and nonpyrochlorelike lattices may be represented. This subtlety also extends to the other characteristics we consider. Regarding lower dimensions, two ICSDs

TABLE I. Of the 55206 ICSD entries of the Materials Flatband Database, here we tabulate the number of unique entries exhibiting lattice structures that are line-graph lattices. Percentages are taken relative to the entire set of Materials Flatband Database entries. We analyze structures either by taking a cut through a Miller plane (2D) or by keeping the entire 3D structure; quasi-2D ICSDs arise from 3D structures without tunneling along one spatial direction. Of these ICSDs, we also note the number with lattices that are not the kagome or pyrochlore lattices, have gapped flat bands, or are conducive to the *S*-matrix method (see main text for additional details). Some ICSDs are represented in multiple columns and some give rise to multiple line-graph-lattice structures that differ in the above characteristics.

	2D	quasi-2D	3D	total
unique materials	3761 (6.81%)	131 (0.24%)	729 (1.32%)	4409 (7.99%)
not kagome or pyrochlorelike	2655	129	$\geqslant$340	$\geqslant$3053
gapped (tight-binding model)	273	7	120	398
S-matrix compatible	5	42	504	551

have the kagome lattice in their quasi-2D layered structure and 1329 ICSDs have the kagome lattice on at least one of their Miller planes. Generally speaking, the pyrochlore and kagome lattices, and those of similar clique compositions, are highly represented among the line-graph lattice structures. These results reflect the fact that these two particular lattices are well known within the condensed matter community.

For the majority of these lattices, the flat bands at -2 are not gapped; however, 120 3D, 7 quasi-2D, and 273 2D ICSDs

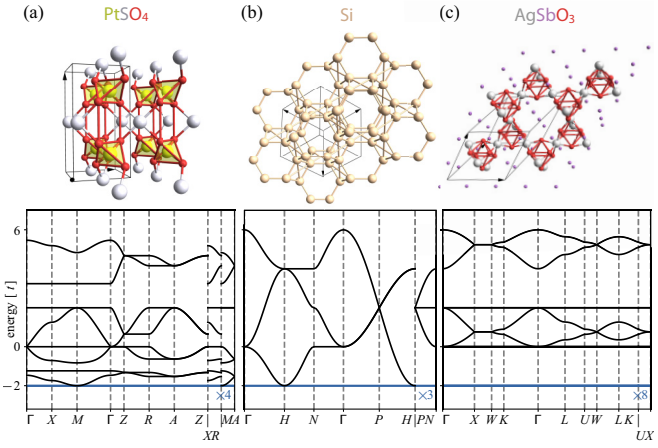

FIG. 3. Crystal and band structures of select 3D line-graph-lattice ICSDs, (a) $PtSO_4$ (ICSD 671491), (b) Si (ICSD 189392), and (c) $AgSbO_3$ (ICSD 25541). In (a), the clique partition is shown via the colored tetrahedra, plus the size-3 (triangle) cliques between two oxygen and one sulfur atom. Because there is an additional atom in the center of each tetrahedron, those cliques are of size 5. The partition for (b) consists entirely of size-4 cliques. The partition for (c) also consists of cliques of size 4, but they are arranged differently and each consists of three oxygen atoms and one silver atom. The antimony atoms are each cliques of size 1, as there are no bonds to other atoms. In all subfigures, unit cells are outlined in black and flat bands in the spectra are highlighted in blue, with the flat-band degeneracy noted.

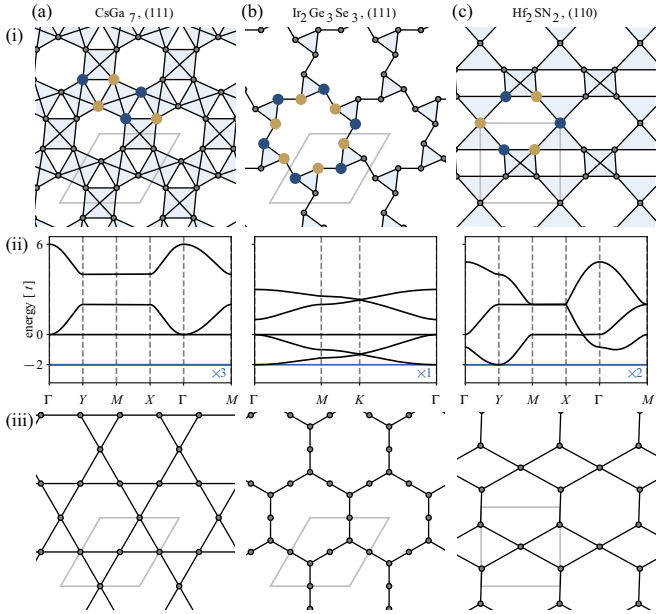

FIG. 4. (i) Crystal structures and representative compact localized state, (ii) band structures, and (iii) root graphs of 2D line-graph lattices coming from (a) $CsGa_7$ (ICSD 102864) along Miller plane (111), (b) $Ir_2Ge_3Se_3$ (ICSD 636733) along (111), and (c) Hf_2SN_2 (ICSD 250915) along (110). (a) is the line graph of the kagome lattice, (b) is the line graph of the split graph of the honeycomb lattice, and (c) is the line graph of a tiling of hexagons and squares. In (i), unit cells are outlined in gray and the cliques of the clique partition are shaded in light blue. The compact localized state is indicated with real-valued amplitudes on the colored sites, where navy (gold) sites indicate positive (negative) amplitude and all amplitudes are equal in magnitude. In (ii), flat bands are highlighted in blue, with flat-band degeneracy noted.

do exhibit gapped flat bands, with gaps up to 2 in units of the tunneling amplitude. In Figs. 3 and 4 we highlight a few examples with and without gapped bands, showing their crystal structure and tight-binding spectra along high-symmetry lines. Figures 3(c) and 4(a) provide examples of 3D and 2D lattices, respectively, which have the maximal gap size found. We additionally include the Krausz partitions and root graphs for the 2D lattices in Fig. 4.

The gappedness and degeneracy of these flat bands can be understood by counting the number of linearly independent flat-band eigenstates, termed "compact localized states" [55,56]. Within the subspace of gapped flat bands, the number of linearly independent compact localized states per unit cell equals the flat-band band degeneracy. If the band is instead ungapped, there will be additional eigenstates at the flat-band energy, each indicating a band touching from dispersive bands [38,40,57]. Figure 4(a) shows representative flat-band eigenstates for our examples. We find lattice structures with band degeneracies from 1 up to 24. Generally speaking, lattices with smaller band degeneracies also have fewer sites per unit cell and therefore may be more amenable to theoretical study.

Given that our tight-binding model naïvely assumes *s*-orbital tunneling and no spin-orbit coupling, we next identify the set of line-graph lattices that can be analyzed using the

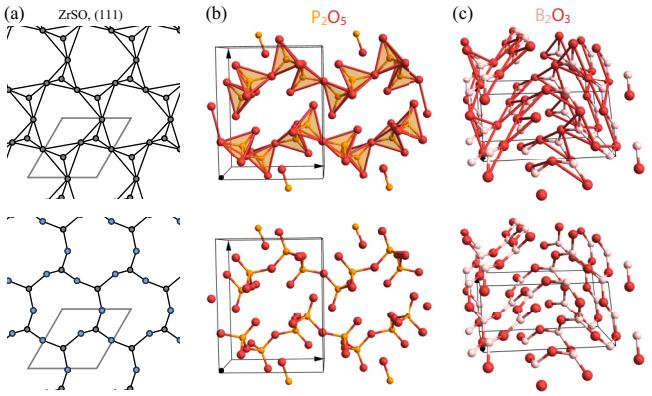

FIG. 5. Example ICSDs to which the S-matrix method applies: (a) ZrSO (ICSD 31721) along Miller plane (111), (b) P_2O_5 (ICSD 36066), and (c) B_2O_3 (ICSD 79698). The top row indicates the lattice structure, which is a line graph, while the bottom row shows how the structure can be decomposed into a bipartite lattice after omitting a subset of bonds.

S-matrix method [48,49]. If a lattice can be decomposed into a bipartite lattice of sublattices A and B, where A contains a greater number of sites than B, then the tight-binding Hamiltonian contains $|A| - |B|$ flat bands in its spectra irrespective of spin or orbital composition [32]. Furthermore, the S-matrix method applies.[1] Then, if the A sublattice is only weakly perturbed by the B sublattice orbitals, then these bands may be (fragile) topological, regardless of its orbital composition and presence or absence of spin-orbit coupling [49]; see Appendix A for details. As shown in the examples of Fig. 5, we find that any given line-graph lattice has a bipartite decomposition if in its Krausz partition, exactly one vertex per clique does not belong to any other cliques. The B sublattice is given by those vertices belonging to only one clique, while the A sublattice is given by the remaining vertices. Upon omitting a subset of bonds in the original line-graph lattice, as shown in the lower row of Fig. 5, the lattice can be made bipartite. Incidentally, this subset consists of the longest bonds in the lattice, implying an shortened effective bond-length cutoff. In total, we find 504 ICSDs in three dimensions, 42 in quasi-two-dimensions, and five in two dimensions that are amenable to a bipartite decomposition and therefore may be analyzed using the S-matrix method.

Many line-graph-lattice materials have the same lattice structure, which may indicate particular line-graph lattices of interest. Table II contains our results determining the number of unique line-graph lattices represented in two dimensions, quasi-two-dimensions, and three dimensions. Of these lattices, the kagome and pyrochlorelike lattices appear most frequently; over 30% of our unique line-graph materials exhibit one of these structures. However, we also find a high degree of representation for the lattices shown in Fig. 6(a). They are the line graph of the Lieb lattice and of the line graph of the 3D Lieb-lattice analog.

[1]While some lattices such as the kagome are not strictly speaking bipartite, they can be obtained as a limit case of the S-matrix method [48].

TABLE II. Because many ICSDs exhibit the same line-graph-lattice structures, here we tabulate the number of unique line-graph lattices found and further categorize them into the ones which are gapped or the ones to which the S-matrix method applies.

	2D	quasi-2D	3D	total
unique lattices	293	$\geqslant$60	$\geqslant$55	$\geqslant$385
gapped	54	$\geqslant$7	$\geqslant$20	$\geqslant$81
S-matrix compatible	4	$\geqslant$9	$\geqslant$7	$\geqslant$18

We characterize these three commonly represented line-graph lattices as follows. The line graph of the Lieb lattice is comprised of one size-4 clique and two size-2 cliques (per unit cell), highlighted in blue in Fig. 6(a). Of its four vertices, all four are adjacent to one size-4 clique and one size-2 clique. This lattice also has one octagon (size-8) face, outlined in blue, around which there are four size-4 and four size-2 cliques in alternating fashion, and each vertex is adjacent to two size-8 faces. The line graph of the 3D Lieb-lattice analog [Fig. 6(a)] has one size-6 clique and three size-2 cliques per unit cell. All six of its vertices are adjacent to one size-6 and one size-2 clique.

Finally, we highlight extracted line-graph lattices, which exhibit gapped flat bands, in contrast to the ungapped flat bands of the kagome and pyrochlore lattices. In Fig. 6(b), we present the line graph of the Cairo tiling and a nonpyrochlore lattice of center-occupied tetrahedra. Four size-3 cliques and two size-4 cliques make up a unit cell of the line graph of the Cairo tiling, where two vertices are adjacent to two size-3 cliques and eight are adjacent to one of each size. There are four pentagon (size-5) faces, outlined in blue, around which

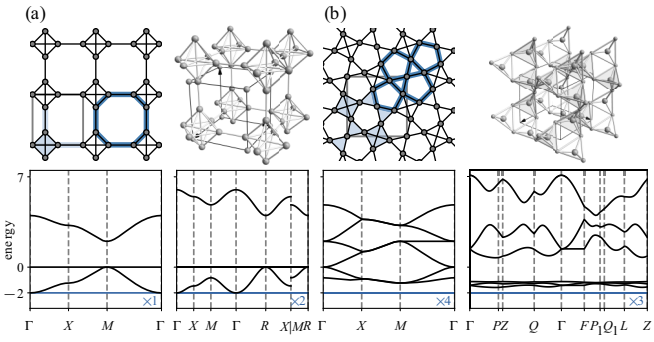

FIG. 6. (a) The line graph of the Lieb lattice and of the 3D Lieb-lattice analog. Apart from the kagome and pyrochlorelike lattices, these are two of the most commonly represented lattices in two dimensions and three dimensions among the 4409 line-graph-lattice ICSDs found, seen in 416 and 71 unique ICSDs, respectively. (b) The line graph of the Cairo tiling and a nonpyrochlore lattice of center-occupied tetrahedra. Unlike the kagome and pyrochlore lattices, the flat bands of these lattices are gapped. The former is seen in 75 ICSDs; the latter is seen in 86 ICSDs. In the top row, unit cells are outlined in gray; in the bottom row, flat bands are highlighted in blue and labeled by their degeneracy. Their characterizations are included in the main text. For the 2D lattices, the cliques and faces referred to in the characterization are highlighted and outlined, respectively.

the size-3 and 4 cliques are interspersed. Each vertex is adjacent to two size-5 faces. Interestingly, the nonpyrochlore lattice is very similar to pyrochlore in that all of its attributes under our filtering algorithm are identical. Yet, its center-occupied tetrahedra (size-5) cliques are arranged in such a way that the tight-binding band spectrum exhibits gapped flat bands. This lattice exemplifies how specific lattice geometries may lead to qualitatively different behavior, even among materials that are stoichiometrically similar.

IV. DISCUSSION

One of the goals of quantum simulation is to solve quantum mechanical problems that cannot be solved with current classical computation. Many such open questions exist within condensed matter, and to this end quantum simulation has made great progress on a multitude of experimental platforms. More specifically, they have provided a mechanism to benchmark and test numerical techniques and theories, giving rise to new intuition and understanding.

Here, we have taken intuition fostered through the development of superconducting-circuit-based quantum simulation and apply it to a search for real-material candidates. Of the 55206 ICSDs examined, almost 8% are found to host line-graph lattices. A full description per ICSD entry of these line-graph lattices is provided in the Materials Flatband Database. These candidates can be probed through condensed matter experiment and may be a starting point for identifying materials that host strongly interacting electrons in flat bands. This work demonstrates how insights gained from working with synthetic matter can lead to actionable results in the search for new quantum materials.

Furthermore, from these ICSDs we have found numerous unique line-graph lattices, which give rise to flat bands due to geometric frustration, rather than a fine-tuning of parameters. Notably, while the kagome and pyrochlore lattices are well known and prevalent examples, they both exhibit ungapped flat bands in their tight-binding spectra. We identify additional line-graph lattices and quantify their prevalence. Of these, we find the line-graph lattices that host gapped flat bands.

Immediate extensions include the development of related algorithms to search for other lattices and families of lattices known to host flat bands. This includes Tasaki's lattices [58], lattices that are constructed entirely from cliques but are not line graphs [59], and decorated or superlattices built from 1D chains [60,61]. Our search can also be run on a database of monolayer materials.

Of course, the line-graph property of a crystalline structure does not directly indicate that the material itself has a flat band, due to orbital and spin degrees of freedom, varied hopping strengths and next-nearest-neighbor hopping, and disorder. However, the properties of these structures can be compared to those of sister materials, which have similar composition but are arranged in the root graph structure. Differences may reveal physics unique to the line-graph flat bands. Indeed, the band spectra of root-graph lattices and their line graphs differ in that only the line graph exhibits flat bands as its lowest bands, but they can otherwise be quite similar. The role of lattice geometry may also be disentangled from other degrees of freedom through comparing materials, which have the same underlying line-graph lattice, but otherwise differ in their symmetry or other aspects. More broadly, these newly highlighted lattices are of particular importance given their potential in designing real and synthetic flat-band materials for studies of strongly correlated many-body physics.

ACKNOWLEDGMENTS

We would like to thank B. Andrei Bernevig, Jens Koch, Aavishkar Patel, and Liujun Zou for helpful discussions. The 3D lattice visualizations in Figs. 3, 5, and 6 were created using the CRYSTALLICA package, developed by Bianca Eifert and Christian Heiliger of Justus Liebig University Giessen and distributed under the MIT License. We acknowledge support from the Princeton Center for Complex Materials NSF DMR-1420541 and from the ARO MURI W911NF-15-1-0397. N.R. has received funding from the European Research Council (ERC) under the European Union's Horizon 2020 research and innovation programme (Grant Agreement No. 101020833).

APPENDIX A: OVERVIEW OF LINE-GRAPH LATTICES

Here we provide a review of line-graph lattices, their flat bands, and the S-matrix method for the reader's convenience. We point those interested in more detail on line-graph lattices to Refs. [1,2,23,37,40,41]. Our S-matrix method discussion summarizes that of Ref. [49] as it relates to line-graph lattices. We also note that a detailed summary is provided in Ref. [48].

1. Line-graph and split-graph lattices

A line-graph lattice is a lattice that results from performing the line-graph operation on some lattice, which we refer to as the root-graph lattice. The operation is as follows:

(i) On every edge of the root-graph lattice, place a vertex of the line-graph lattice.

(ii) Add edges between these newly placed vertices if their corresponding edges (in the root graph) are adjacent, i.e., if they share a vertex in the root graph.

A schematic of this is shown in Fig. 7(a).

Now consider a split-graph lattice: this results from the following operation, shown in Fig. 7(b).

(i) Replace every edge of the root-graph lattice with two edges connected by a vertex.

The split-graph lattice and line-graph lattice are related to each other. More specifically, we label newly added vertices as belonging to set A and original (root-graph) vertices as belonging to set B. Then we can obtain the line-graph lattice by considering all sites in A, plus second-order tunnelings to unique A sites through B sites. Notice also that because sites in A only tunnel to sites in B and vice-versa, the split-graph lattice is bipartite.

2. Line-graph-lattice flat bands

In this section, we prove that line-graph lattices in dimensions greater than one exhibit flat bands at energy -2 (in units of the tunneling energy), using the labeling of the previous section.

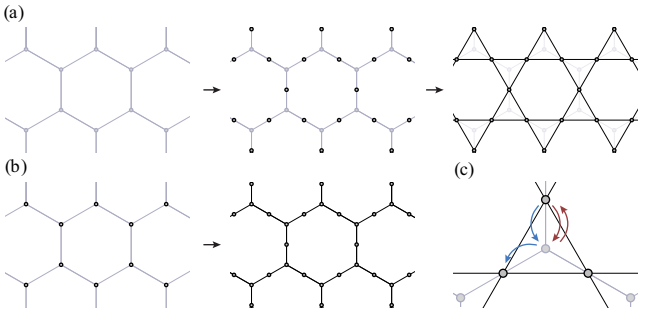

FIG. 7. Schematics for the (a) line-graph-lattice and (b) split-graph-lattice constructions described in Appendix A 1, using the example of the honeycomb lattice as the root graph. Each arrow corresponds to a step of the construction. The final line-graph (split-graph) lattice consists of the black vertices and edges in the final panel of (a) [(b)]. (c) Second-order hopping contributions to the effective Hamiltonian $T_{\mathbf{k}}$. Blue arrows show hopping between two distinct sites in A (black sites), mediated by a B-site (gray sites) that is a nearest-neighbor to both. Red arrows show hopping between a site in A, to a neighboring site in B, and back to the same site in A.

First, we confirm that the number of sites in A is greater than that of B. In the line-graph construction, the number of sites in A is equal to the number of edges in the original root graph, and the number of sites in B is equal to the number of sites in the root graph. Every root-graph vertex contributes $d/2$ edges, where d is the number of edges coming out of that vertex. For the sake of counting, we can ignore $d = 1$ vertices and their adjacent edge (these contribute an equal number of edges and sites). Then for all remaining vertices, $d \geqslant 2$. Because the lattice has dimensionality greater than one, there must exist vertices for which $d > 2$. Hence in total there must be more edges than vertices, and $|A| > |B|$.

Second, consider the $|A| \times |B|$ matrix $S_{\mathbf{k}}$ in momentum space $\mathbf{k}$ that indicates the hopping between subsets A and B. Being rectangular, this matrix has rank at most equal to its smallest dimension ($|B|$), leaving at least $|A| - |B|$ vectors in the null space. Now consider the effective Hamiltonian $T_{\mathbf{k}} = S_{\mathbf{k}} S_{\mathbf{k}}^{\dagger}$. This Hamiltonian reflects hopping from sites in A to sites in B, then back to A. We also know that $\mathrm{rank}(T_{\mathbf{k}}) = \mathrm{rank}(S_{\mathbf{k}} S_{\mathbf{k}}^{\dagger}) = \mathrm{rank}(S_{\mathbf{k}}) = |B|$. Thus there are (at least) $|A| - |B|$ flat bands at zero in the spectrum of $T_{\mathbf{k}}$.

Finally, we connect the Hamiltonian $T_{\mathbf{k}}$ to the tight-binding model on a line-graph lattice. As depicted schematically in Fig. 7(c), there will be two types of contributions in $T_{\mathbf{k}}$. The first maps hopping between two distinct sites in A (mediated by hopping through a B site that is a nearest neighbor to both). The second maps hopping between each site in A, to a neighboring site in B, and back to the original site in A. Notably, the first contribution yields exactly the line-graph lattice Hamiltonian. It remains, then, to evaluate the second contribution.

Notice that by construction, all sites in A have exactly two nearest neighbors in B. If hopping is isotropic (we have only an s orbital on each site), then this second contribution is simply $2 \cdot \mathbb{1}_{|A|}$, corresponding to an overall energy offset. In the line-graph-lattice Hamiltonian, then, the $|A| - |B|$ flat bands are shifted to energy -2.

3. *S*-matrix method

In this section we summarize the S-matrix method and main conclusions. This formalism applies to bipartite crystalline lattices and has been used to show that the flat bands of such lattices may be (fragile) topological, even with spin and orbital degrees of freedom. We begin with the tight-binding Hamiltonian $H_{\mathbf{k}}$ in momentum space of a bipartite lattice:

$$H_{\mathbf{k}} = \begin{pmatrix} \mathbb{1} & S_{\mathbf{k}} \\ S_{\mathbf{k}}^{\dagger} & \mathbb{1} \end{pmatrix} \begin{matrix} \overleftrightarrow{|B|} \\ \updownarrow |A| \end{matrix}, \tag{A1}$$

where $S_{\mathbf{k}}$ is the $|A| \times |B|$ matrix indicating the hopping between the two subsets. Notably, this hopping can include spin and orbital degrees of freedom.

We know that this Hamiltonian gives (at least) $|A| - |B|$ flat bands at zero energy [32]. Indeed, the rank of this Hamiltonian is at most $2|B|$; the rank of the upper $|A|$ rows is limited by the rank of $S_{\mathbf{k}}$, which is at most $|B|$, while the lower $|B|$ rows can have full rank. The nullity is thus at least $|A| - |B|$, given by the difference between the number of rows (or columns) of the Hamiltonian and its rank. This corresponds to at least $|A| - |B|$ flat bands at zero energy.

Now we focus on the main result from the S-matrix method: the topology of these flat bands. This begins by taking the singular value decomposition (SVD) of $S_{\mathbf{k}}$:

$$S_{\mathbf{k}} = W_{\mathbf{k}} \Sigma_{\mathbf{k}} V_{\mathbf{k}}^{\dagger}. \tag{A2}$$

Here $W_{\mathbf{k}}$ ($V_{\mathbf{k}}$) is an $|A| \times |A|$ ($|B| \times |B|$) matrix, while $\Sigma_{\mathbf{k}}$ is a diagonal $|A| \times |B|$ matrix of the singular values. Additionally, the columns of $W_{\mathbf{k}}$ ($V_{\mathbf{k}}$) are the left- (right-)singular vectors of $S_{\mathbf{k}}$, which we can write as $\phi_{\mathbf{k},\alpha}$ ($\psi_{\mathbf{k},\alpha}$) where α enumerates the columns and can take values between 1 and the rank $r_{\mathbf{k}}$. Then the SVD takes the form:

$$S_{\mathbf{k}} = \sum_{\alpha=1}^{r_{\mathbf{k}}} \epsilon_{\mathbf{k},\alpha} \phi_{\mathbf{k},\alpha} \psi_{\mathbf{k},\alpha}^{\dagger}. \tag{A3}$$

It is then straightforward to show that the eigenvectors of $H_{\mathbf{k}}$ are given by:

$$\Psi_{\mathbf{k},\alpha}^{\pm} = \begin{cases} \frac{1}{\sqrt{2}} \begin{pmatrix} \pm\phi_{\mathbf{k},\alpha} \\ \psi_{\mathbf{k},\alpha} \end{pmatrix} & 1 \leqslant \alpha \leqslant r_{\mathbf{k}} \\ \begin{pmatrix} \phi_{\mathbf{k},\alpha} \\ 0 \end{pmatrix} & r_{\mathbf{k}} < \alpha \leqslant |A| \end{cases} \tag{A4}$$

with eigenvalues $\pm\epsilon_{\mathbf{k},\alpha}$ and 0, respectively.

Now consider the effective Hamiltonians $T_{A,\mathbf{k}} = S_{\mathbf{k}} S_{\mathbf{k}}^{\dagger}$ and $T_{B,\mathbf{k}} = S_{\mathbf{k}}^{\dagger} S_{\mathbf{k}}$. The first Hamiltonian reflects hopping from sites in A to sites in B, then back to A, while the second reflects hopping from B to A to B. The resulting SVDs are

$$T_{A,\mathbf{k}} = \sum_{\alpha=1}^{r_{\mathbf{k}}} \epsilon_{\mathbf{k},\alpha}^2 \phi_{\mathbf{k},\alpha} \phi_{\mathbf{k},\alpha}^{\dagger} \tag{A5}$$

$$T_{B,\mathbf{k}} = \sum_{\alpha=1}^{r_{\mathbf{k}}} \epsilon_{\mathbf{k},\alpha}^2 \psi_{\mathbf{k},\alpha} \psi_{\mathbf{k},\alpha}^{\dagger}. \tag{A6}$$

We first note that $T_{A,\mathbf{k}}$ is identical to $T_{\mathbf{k}}$ from the previous section, which hosts at least $|A| - |B|$ flat bands at zero, irrespective of orbital or spin degrees of freedom. These effective Hamiltonians describe hopping on the bipartite lattice in the case that second-order hopping dominates over nearest-neighbor hopping. Thus if the on-site energy difference between A sites and B sites is sufficiently large, then $T_{A,\mathbf{k}}$ describes the effective Hamiltonian on A sites, $T_{B,\mathbf{k}}$ describes the effective Hamiltonian on B sites, and hopping between A and B sites can be treated perturbatively.

From Eqs. (A5) and (A6) we can conclude:

(i) The eigenvectors of $T_{A,\mathbf{k}}$ are $\phi_{\mathbf{k},\alpha}$, i.e., the left-singular vectors of $S_{\mathbf{k}}$, for $1 \leqslant \alpha \leqslant r_{\mathbf{k}}$, which includes the $|A| - |B|$ vectors corresponding to the flat bands at zero energy.

Crucially, this means that the flat-band eigenfunctions of $H_{\mathbf{k}}$ and $T_{A,\mathbf{k}}$ are identical [up to padding by zeros as seen in Eq. (A4)].

(ii) The eigenvectors of $T_{B,\mathbf{k}}$ are $\psi_{\mathbf{k},\alpha}$, i.e., the right-singular vectors of $S_{\mathbf{k}}$.

(iii) For every eigenvector $\phi_{\mathbf{k},\alpha}$ of $T_{A,\mathbf{k}}$ with eigenenergy $\epsilon^2_{\mathbf{k},\alpha}$, $\psi_{\mathbf{k},\alpha} = \frac{1}{\epsilon_{\mathbf{k},\alpha}} S^\dagger_{\mathbf{k}} \phi_{\mathbf{k},\alpha}$ is an eigenvector of $T_{B,\mathbf{k}}$ with the same eigenenergy. In other words, $T_{A,\mathbf{k}}$ and $T_{B,\mathbf{k}}$ have the same dispersive bands in the spectra.

As the A sites of $T_{A,\mathbf{k}}$ and the B sites of $T_{B,\mathbf{k}}$ are subsets of the bipartite lattice sites of $H_{\mathbf{k}}$, in most cases they will all belong to the same site-symmetry group. This means that the equivalent bands and wave functions across these three matrices can be used interchangeably to determine properties of band representation and topology.

Finally, topological quantum chemistry (TQC) [50] and its extension to magnetic TQC [62] can be used to analyze the topology of the flat bands. The main idea here is to identify bands whose wave functions cannot all be described by exponentially localized Wannier functions and are therefore topological. This is done through a formalism characterizing all trivial atomic bands by elementary band representations (EBRs), based upon the lattice symmetry, orbitals, and orbital locations. A set of bands whose representation is given by a linear combination of EBRs with positive integer coefficients is trivial. For example, the entire set of bands in the spectra of $T_{A,\mathbf{k}}$ must be trivial because they are described by the orbitals localized on the A sites. Similarly, the entire set of bands in the spectra of $T_{B,\mathbf{k}}$ is trivial. By contrast, a set of bands is fragile topological if their representation is a linear combination of EBRs where at least one coefficient must be a negative integer.

The representation of a band is directly related to its eigenstates at high-symmetry points in the Brillouin zone. More specifically, it is related to how these states transform under the symmetries of those high-symmetry points; this is encapsulated through (co)irreducible representations [(co)irreps]. Because the bipartite lattice and its sublattices all have the same symmetries, the same symmetry operators can be applied independently to each of these lattices. Then, using the enumerated conclusions above, it can be shown that eigenstates $\phi_{\mathbf{k},\alpha}$ of $T_{A,\mathbf{k}}$ with eigenenergy $\epsilon^2_{\mathbf{k},\alpha}$ will generally transform in the same way [with the same (co)irreps] as eigenstates $\psi_{\mathbf{k},\alpha}$ of $T_{B,\mathbf{k}}$ with the same eigenenergy. Exceptions occur for eigenstates with energy zero (at some specific momentum or for all momenta), where there is no valid mapping between $\phi_{\mathbf{k},\alpha}$ and $\psi_{\mathbf{k},\alpha}$. The topology of the flat bands of $T_{A,\mathbf{k}}$ then follows from the formal (co)irrep difference of the bands of $T_{A,\mathbf{k}}$ and $T_{B,\mathbf{k}}$. Moreover, the flat bands of $H_{\mathbf{k}}$ will have the same topology. This difference can also be used to determine whether any band touching points between the flat and dispersive bands in $T_{A,\mathbf{k}}$ (and equivalently $H_{\mathbf{k}}$) are symmetry protected.

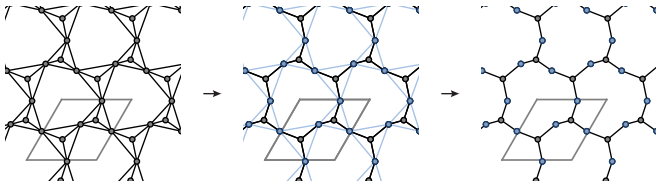

FIG. 8. Criteria for a line-graph lattice to be S-matrix compatible. Taking the example from Fig. 5(a) of the main text, we see that each clique consists of four vertices, given by each triangle, the center vertex, and the connecting edges. The center vertex is only part of one clique (subset B). We identify vertices that are part of two cliques (subset A), colored in blue, and the edges connecting these vertices, also colored in blue. After removing these edges, the resulting lattice is bipartite.

In particular, Ref. [49] considers all possible differences of EBRs (that can only be represented as a difference). This is the set of all fragile topological bands. The authors show that for any of these representations, a bipartite lattice can be constructed whose flat bands are gapped and have that representation. Therefore, among bipartite lattices where the A and B sites' on-site energies are well separated and the flat bands are gapped, there exist lattices whose flat bands are fragile topological. As a result, identifying materials with bipartite-lattice crystalline structures is a promising step towards realizing and probing fragile topological flat bands.

4. *S*-matrix-compatible line-graph-lattice crystal structures

The exactly flat bands of line-graph lattices assume s orbitals on every site and no spin-orbit coupling or time-reversal symmetry breaking. However, the S-matrix method formalism shows that bipartite crystalline lattices can host exactly flat topological bands, generalizable across orbital compositions and the presence or absence of spin-orbit coupling or time-reversal symmetry breaking. Although line-graph lattices beyond one dimension are not bipartite, a subset of them are closely related to bipartite lattices. Thus, our high-throughput search for line-graph-lattice materials can straightforwardly be extended to identify those that are bipartite under modified bond-cutoff parameters and are therefore S-matrix compatible.

Here we elaborate on the material structure criteria that determines this subset of lattices. As discussed in the main text, a given lattice is a line-graph lattice if and only if it has a Krausz-(2, 1) partition. This means that the lattice can be divided into fully connected subgraphs (cliques) where each vertex is part of at most two cliques and each edge is part of exactly one clique.

Now consider lattices where for each clique, there exists exactly one vertex, which is part of only one clique, for example Fig. 5(a) of the main text, which is copied in Fig. 8 here. If all edges are omitted between vertices that are part of two

cliques, as seen in Fig. 8, then every remaining edge must connect a vertex belonging to two cliques, to a vertex belonging to one. In other words, taking the set of two-clique vertices as A and the set of one-clique vertices as B, we have created a bipartite lattice: sites in A only tunnel to sites in B and vice-versa. Thus the S-matrix method applies to these lattices.

APPENDIX B: ALGORITHM

Here we provide additional details on the algorithm used to determine which materials have line-graph-lattice crystalline structures. Broadly speaking, the algorithm can be split into four parts. First, we determine the cutoff bond length and optionally take a cut through a Miller plane. Second, we filter out lattices that have dimensionality below two dimensions, as well as lattices whose numbers of edges and vertices prohibit a Krausz partition. Third, we reduce the translationally invariant lattice to a finite-sized graph. Finally, we extract the cliques present as subgraphs of our graph and determine whether a Krausz-(2, 1) partition exists.

We note that this is not the only way to determine whether a given lattice is a line graph. For example, there are nine forbidden minimal subgraphs; if a subset of vertices of the graph, combined with all edges of the graph connecting those vertices, creates one of these forbidden subgraphs, then the candidate graph cannot be a line graph [63]. However, our chosen algorithm for line-graph testing offers ways to subsequently characterize the detected line graphs. It can also be straightforwardly extended and applied to lattices.

1. Parameters

Following Ref. [48], we determine our bond cutoff length through two parameters: a maximum allowed bond length m and an overall multiplicative coefficient c. After calculating the minimum distance d between any two atoms in the lattice, we create bonds between any two atoms, which are closer than the distance $c \cdot \max(m, d)$. We examine all lattices resulting from $m \in \{1.5, 1.8, 2.1, 2.4, 2.7\}$ Å and $c \in \{1.2, 1.5, 1.7\}$.

For each lattice, we test the full 3D lattice as well as those along each of its Miller planes. In these planes, bonds between atoms are inherited from the 3D lattice. Symmetrically redundant Miller planes, identified via the PYMATGEN package [64–66], are omitted.

The results of our algorithm will, of course, depend on the exact criteria used to determine bond connectivity. To reflect this, we have included in Table III the number of unique ICSDs with line-graph-lattice crystalline structures given all (m, c) parameters studied in this work, sorted by lattice dimension. There exist many other algorithms for bond connectivity, as well as benchmark evaluations against experiment [67]. Future directions include exploring such algorithms and how they impact the results of our line-graph-lattice screening. For example, ICSDs can be further screened for ones that exhibit line-graph-lattice structures that are more robust to choice of bond determination algorithm.

TABLE III. As expected, the exact bond cutoff parameters used affect the ICSDs identified to have line-graph-lattice structures. This table enumerates the number of unique ICSDs with such structures, for each combination of minimum distance parameter m and cutoff coefficient c. These parameters are used to determine the bond cutoff.

m (Å)	c	2D	quasi-2D	3D
1.5	1.2	140	10	14
1.5	1.5	781	30	56
1.5	1.7	954	34	422
1.8	1.2	5	4	5
1.8	1.5	83	17	57
1.8	1.7	191	4	105
2.1	1.2	17	7	5
2.1	1.5	259	5	14
2.1	1.7	723	0	0
2.4	1.2	250	20	82
2.4	1.5	513	1	2
2.4	1.7	1283	1	0
2.7	1.2	356	7	6
2.7	1.5	792	0	3
2.7	1.7	1846	0	0

2. Filtering

Our first filtering stage consists of examining the connectivities of the vertices to determine whether atomic bonding occurs across two or more dimensions. For example, if the bond distance is sufficiently small, there may be clusters of atoms that are locally connected, but not connected across unit cells; these lattices are omitted from our search. Lattices on Miller planes must extend over the full two dimensions, while for full 3D lattices we keep those extending across two or three dimensions.

Regarding the second filtering stage, note that given a lattice with v vertices per unit cell, the minimum number of edges e allowed for a Krausz partition is $e_{\min} = 0$. This is the trivial case where each vertex is in its own clique of size 1. The maximum number of edges is $e_{\max} = v \cdot (2v - 1)$. This follows from the fact that a clique with v' vertices has $\frac{v' \cdot (v'-1)}{2}$ edges. Each vertex can be part of two cliques, but the two cliques need not be discrete. Thus, the maximal number of edges results from having only a single clique of $v' = 2v$ vertices, where each vertex of the unit cell is represented exactly twice. This single clique then has $v \cdot (2v - 1)$ edges. By applying this very conservative filter, we eliminate lattices with an impractical number of edges.

3. Reduction to finite-sized graph

The goal of this step of the algorithm is to convert the lattice into a finite-sized graph, such that the graph is a line graph if and only if the lattice is a line-graph lattice. Thus, it is sufficient to create a finite-sized graph that, when translated along the lattice vectors, reproduces the entire lattice. The number of edges of the graph is then given by the number of edges in the unit cell; however, the number of vertices may be greater than the number of sites per unit cell. As an example, see Fig. 9, which shows the reduction process for the line graph of the kagome lattice. These additional vertices will have counterparts in the graph, separated by integer numbers of the lattice vectors. As a result, we first take the lattice adjacency list and represent it as if it were a finite-sized graph,

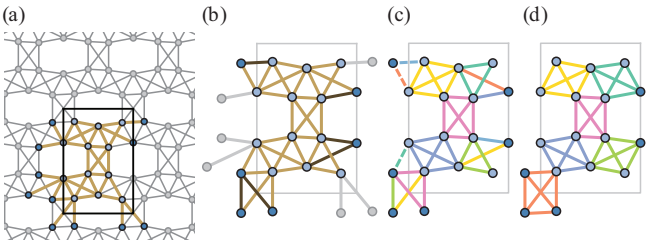

FIG. 9. Reduction and Kraus partition search for the line graph of the kagome lattice. (a) Translationally invariant lattice in gray, with isolated edges and vertices (colored) for the initial reduction to a finite-sized graph. (b) Translation of edges along lattice vectors to increase the number of triangle subgraphs. The goal is to create a graph, which is a line graph if and only if the original lattice is a line-graph lattice. Gray edges are translated to the dark brown ones, upon which gray vertices are removed. (c) Failed attempt at a Krausz partition, indicated by the colored cliques, with dashed edges indicating ambiguous edges, see text for details. (d) Successful Krausz partition upon moving the ambiguous edges. In all subfigures, the outlined rectangle indicates the unit cell and lattice vectors.

where translationally invariant vertices (in neighboring unit cells) are labeled as unique.

In Fig. 9(a), this is done by considering all sites within a single unit cell, colored in light blue, along with one translationally invariant copy of all edges incident on those sites (gold) and their incident vertices. While the number of edges is equal to the number per unit cell, this is not the case for the total set of vertices. The dark blue vertices lie outside of the unit cell outlined in black, i.e., each is translationally invariant from one of the light blue vertices. In creating the finite-sized graph, however, these sites are treated as separate vertices.

We then further manipulate the graph by moving edges and vertices by integer multiples of the lattice vectors, to create a graph, which is as similar to a line graph as possible. More specifically, fully connected subgraphs (cliques) consist of many triangles formed by three edges. Thus our algorithm preferentially translates edges and sets of edges to create clusters of triangles with shared edges. Figure 9(b) shows how the original edges of Fig. 9(a) can be moved from the light-gray locations to the dark brown ones. This reduces the number of vertices with only one incident edge, which is equivalent to reducing the total number of vertices in the graph.

In some cases, even after this optimization there remain ambiguities regarding how a subset of edges should be translated. In Fig. 9(c), these are shown as the three dashed edges. This requires that we search for a Krausz partition for each possible combination of translations, exhibiting exponential scaling with the number of ambiguous edges. As a result, we set an upper limit for the number of possibilities accepted, below which we check for a Krausz partition among all possible arrangements. Through examining the tight-binding model band spectra, we estimate that this cutoff leaves undetected at most one 2D and 27 quasi-2D and 3D line-graph materials.

4. Krausz partition search

Our algorithm determines whether the graph is a line graph by first identifying all maximal cliques of the graph. This is done with the Bron-Kerbosh algorithm [53]. Then, we determine whether a subset of these cliques fulfills the conditions of a Krausz partition: all edges are part of exactly one clique, while each vertex is part of at most two cliques. As a subtlety, there are cases in which a clique of size 3 ought to be instead represented as a clique of size 2, plus two edges and a vertex that are part of other cliques; we necessarily take cases such as these into consideration.

The graph in Fig. 9(c) does not admit a Krausz partition, as seen from an attempt to color the cliques of the graph. Note that in Fig. 9(c), colors are reused for visibility and disjoint subgraphs of the same coloring represent separate cliques. Multiple vertices of this graph are contained within more than two cliques. In contrast, upon translating the three ambiguous (dashed) edges, in Fig. 9(d) we find that we can create a graph, which is indeed a line graph. Notice that because the number of vertices is still greater than the number per unit cell, some vertices are represented in duplicate. As a result, in determining whether a Krausz partition exists, the number of adjacent cliques must be summed for these equivalent vertices.

[1] A. Mielke, Ferromagnetic ground states for the Hubbard model on line graphs, J. Phys. A: Math. Gen. **24**, L73 (1991).
[2] A. Mielke, Ferromagnetism in the Hubbard model on line graphs and further considerations, J. Phys. A: Math. Gen. **24**, 3311 (1991).
[3] H. Tasaki, Ferromagnetism in the Hubbard Models with Degenerate Single-Electron Ground States, Phys. Rev. Lett. **69**, 1608 (1992).
[4] H. Tasaki, Hubbard model and the origin of ferromagnetism, Eur. Phys. J. B **64**, 365 (2008).
[5] C. Danieli, A. Andreanov, and S. Flach, Many-body flatband localization, Phys. Rev. B **102**, 041116(R) (2020).
[6] M. Daumann, R. Steinigeweg, and T. Dahm, Many-Body localization in translational invariant diamond ladders with flat bands, arXiv:2009.09705v1.
[7] Y. Kuno, T. Orito, and I. Ichinose, Flat-band many-body localization and ergodicity breaking in the Creutz ladder, New J. Phys. **22**, 013032 (2020).
[8] R. Khare and S. Choudhury, Localized dynamics following a quantum quench in a non-integrable system: An example on the sawtooth ladder, J. Phys. B **54**, 015301 (2021).
[9] N. Roy, A. Ramachandran, and A. Sharma, Interplay of disorder and interactions in a flat-band supporting diamond chain, Phys. Rev. Res. **2**, 043395 (2020).
[10] T. Orito, Y. Kuno, and I. Ichinose, Non-thermalized dynamics of flat-band many-body localization, Phys. Rev. B **103**, L060301 (2021).
[11] F. Xie, Z. Song, B. Lian, and B. A. Bernevig, Topology-Bounded Superfluid Weight in Twisted Bilayer Graphene, Phys. Rev. Lett. **124**, 167002 (2020).

[12] X. Hu, T. Hyart, D. I. Pikulin, and E. Rossi, Geometric and Conventional Contribution to the Superfluid Weight in Twisted Bilayer Graphene, Phys. Rev. Lett. **123**, 237002 (2019).

[13] A. Julku, T. J. Peltonen, L. Liang, T. T. Heikkilä, and P. Törmä, Superfluid weight and Berezinskii-Kosterlitz-Thouless transition temperature of twisted bilayer graphene, Phys. Rev. B **101**, 060505(R) (2020).

[14] T. Hazra, N. Verma, and M. Randeria, Bounds on the Superconducting Transition Temperature: Applications to Twisted Bilayer Graphene and Cold Atoms, Phys. Rev. X **9**, 031049 (2019).

[15] T. Neupert, L. Santos, C. Chamon, and C. Mudry, Fractional Quantum Hall States at Zero Magnetic Field, Phys. Rev. Lett. **106**, 236804 (2011).

[16] Y.-F. Wang, H. Yao, C.-D. Gong, and D. N. Sheng, Fractional quantum Hall effect in topological flat bands with Chern number two, Phys. Rev. B **86**, 201101(R) (2012).

[17] N. Regnault and B. A. Bernevig, Fractional Chern Insulator, Phys. Rev. X **1**, 021014 (2011).

[18] K. Sun, Z. Gu, H. Katsura, and S. Das Sarma, Nearly Flatbands with Nontrivial Topology, Phys. Rev. Lett. **106**, 236803 (2011).

[19] D. Leykam, A. Andreanov, and S. Flach, Artificial flat band systems: from lattice models to experiments, Adv. Phys.: X **3**, 1473052 (2018).

[20] F. Baboux, L. Ge, T. Jacqmin, M. Biondi, E. Galopin, A. Lemaître, L. Le Gratiet, I. Sagnes, S. Schmidt, H. E. Türeci, A. Amo, and J. Bloch, Bosonic Condensation and Disorder-Induced Localization in a Flat Band, Phys. Rev. Lett. **116**, 066402 (2016).

[21] S. Mukherjee, M. DiLiberto, P. Öhberg, R. R. Thomson, and N. Goldman, Experimental Observation of Aharonov-Bohm Cages in Photonic Lattices, Phys. Rev. Lett. **121**, 075502 (2018).

[22] J. Ma, J.-W. Rhim, L. Tang, S. Xia, H. Wang, X. Zheng, S. Xia, D. Song, Y. Hu, Y. Li, B.-J. Yang, D. Leykam, and Z. Chen, Direct Observation of Flatband Loop States Arising from Nontrivial Real-Space Topology, Phys. Rev. Lett. **124**, 183901 (2020).

[23] A. J. Kollár, M. Fitzpatrick, and A. A. Houck, Hyperbolic lattices in circuit quantum electrodynamics, Nature (London) **571**, 45 (2019).

[24] J. S. C. Hung, J. H. Busnaina, C. W. Sandbo Chang, A. M. Vadiraj, I. Nsanzineza, E. Solano, H. Alaeian, E. Rico, and C. M. Wilson, Quantum Simulation of the Bosonic Creutz Ladder with a Parametric Cavity, Phys. Rev. Lett. **127**, 100503 (2021).

[25] G. B. Jo, J. Guzman, C. K. Thomas, P. Hosur, A. Vishwanath, and D. M. Stamper-Kurn, Ultracold atoms in a tunable optical kagome lattice, Phys. Rev. Lett. **108**, 045305 (2012).

[26] Y. He, R. Mao, H. Cai, J.-X. Zhang, Y. Li, L. Yuan, S.-Y. Zhu, and D.-W. Wang, Flat-band localization in Creutz superradiance lattices, Phys. Rev. Lett. **126**, 103601 (2021).

[27] R. Bistritzer and A. H. Macdonald, Moiré bands in twisted double-layer graphene, Proc. Natl. Acad. Sci. **108**, 12233 (2011).

[28] D. Marchenko, D. V. Evtushinsky, E. Golias, A. Varykhalov, T. Seyller, and O. Rader, Extremely flat band in bilayer graphene, Sci. Adv. **4**, eaau0059 (2018).

[29] Z. Zhang, Y. Wang, K. Watanabe, T. Taniguchi, K. Ueno, E. Tutuc, and B. J. LeRoy, Flat bands in twisted bilayer transition metal dichalcogenides, Nature Phys. **16**, 1093 (2020).

[30] M. Iqbal Bakti Utama, R. J. Koch, K. Lee, N. Leconte, H. Li, S. Zhao, L. Jiang, J. Zhu, K. Watanabe, T. Taniguchi, P. D. Ashby, A. Weber-Bargioni, A. Zettl, C. Jozwiak, J. Jung, E. Rotenberg, A. Bostwick, and F. Wang, Visualization of the flat electronic band in twisted bilayer graphene near the magic angle twist, Nature Phys. **17**, 184 (2021).

[31] S. Lisi, X. Lu, T. Benschop, T. A. de Jong, P. Stepanov, J. R. Duran, F. Margot, I. Cucchi, E. Cappelli, A. Hunter, A. Tamai, V. Kandyba, A. Giampietri, A. Barinov, J. Jobst, V. Stalman, M. Leeuwenhoek, K. Watanabe, T. Taniguchi, L. Rademaker *et al.*, Observation of flat bands in twisted bilayer graphene, Nature Phys. **17**, 189 (2021).

[32] E. H. Lieb, Two Theorems on the Hubbard Model, Phys. Rev. Lett. **62**, 1201 (1989).

[33] S. Flach, D. Leykam, J. D. Bodyfelt, P. Matthies, and A. S. Desyatnikov, Detangling flat bands into Fano lattices, Europhys. Lett. **105**, 30001 (2014).

[34] Y. Xu and H. Pu, Building flat-band lattice models from Gram matrices, Phys. Rev. A **102**, 053305 (2020).

[35] I. Syozi, Statistics of Kagome Lattice, Prog. Theor. Phys. **6**, 306 (1951).

[36] M. A. Subramanian, G. Aravamudan, and G. V. Subba Rao, Oxide pyrochlores—A review, Prog. Solid State Chem. **15**, 55 (1983).

[37] D. Cvetkovic, P. Rowlinson, and S. Simic, *Spectral Generalizations of Line Graphs* (Cambridge University Press, Cambridge, 2004).

[38] A. J. Kollár, M. Fitzpatrick, P. Sarnak, and A. A. Houck, Line-graph lattices: Euclidean and non-euclidean flat bands, and implementations in circuit quantum electrodynamics, Commun. Math. Phys. **376**, 1909 (2020).

[39] I. Carusotto, A. A. Houck, A. J. Kollár, P. Roushan, D. I. Schuster, and J. Simon, Photonic materials in circuit quantum electrodynamics, Nature Phys. **16**, 268 (2020).

[40] C. S. Chiu, D.-S. Ma, Z.-D. Song, B. A. Bernevig, and A. A. Houck, Fragile topology in line-graph lattices with two, three, or four gapped flat bands, Phys. Rev. Res. **2**, 043414 (2020).

[41] D.-S. Ma, Y. Xu, C. S. Chiu, N. Regnault, A. A. Houck, Z. Song, and B. A. Bernevig, Spin-Orbit-Induced Topological Flat Bands in Line and Split Graphs of Bipartite Lattices, Phys. Rev. Lett. **125**, 266403 (2020).

[42] Z. Liu, F. Liu, and Y. S. Wu, Exotic electronic states in the world of flat bands: From theory to material, Chin. Phys. B **23**, 077308 (2014).

[43] V. Elser, Nuclear Antiferromagnetism in a Registered ^{3}He Solid, Phys. Rev. Lett. **62**, 2405 (1989).

[44] M. B. Hastings, Dirac structure, RVB, and Goldstone modes in the kagomé antiferromagnet, Phys. Rev. B **63**, 014413 (2000).

[45] M. Kang, L. Ye, S. Fang, J. S. You, A. Levitan, M. Han, J. I. Facio, C. Jozwiak, A. Bostwick, E. Rotenberg, M. K. Chan, R. D. McDonald, D. Graf, K. Kaznatcheev, E. Vescovo, D. C. Bell, E. Kaxiras, J. van den Brink, M. Richter, M. Prasad Ghimire *et al.*, Dirac fermions and flat bands in the ideal kagome metal FeSn, Nature Mater. **19**, 163 (2020).

[46] M. Kang, S. Fang, L. Ye, H. C. Po, J. Denlinger, C. Jozwiak, A. Bostwick, E. Rotenberg, E. Kaxiras, J. G. Checkelsky, and R. Comin, Topological flat bands in frustrated kagome lattice CoSn, Nature Commun. **11**, 4004 (2020).

[47] I. Hase, T. Yanagisawa, and K. Kawashima, Flat-band in pyrochlore oxides: A first-principles study, Nanomaterials **9**, 876 (2019).

[48] N. Regnault, Y. Xu, M.-R. Li, D.-S. Ma, M. Jovanovic, A. Yazdani, S. S. P. Parkin, C. Felser, L. M. Schoop, N. P. Ong, R. J. Cava, L. Elcoro, Z.-D. Song, and B. A. Bernevig, Catalogue of flat band stoichiometric materials, arXiv:2106.05287v1.

[49] D. Călugăru, A. Chew, L. Elcoro, Y. Xu, N. Regnault, Z.-D. Song, and B. A. Bernevig, General construction and topological classification of all magnetic and non-magnetic flat bands, Nat. Phys. **18**, 185 (2022).

[50] B. Bradlyn, L. Elcoro, J. Cano, M. G. Vergniory, Z. Wang, C. Felser, M. I. Aroyo, and B. A. Bernevig, Topological quantum chemistry, Nature (London) **547**, 298 (2017).

[51] M. G. Vergniory, B. J. Wieder, L. Elcoro, S. S. P. Parkin, C. Felser, B. A. Bernevig, and N. Regnault, All topological bands of all stoichiometric materials, arXiv:2105.09954v1.

[52] J. Krausz, Démonstration nouvelle d'un théorème de Whitney sur les réseaux, Matematikai Fizikai Lapok **50**, 75 (1943).

[53] C. Bron and J. Kerbosch, Algorithm 457: Finding all cliques of an undirected graph, Commun. ACM **16**, 575 (1973).

[54] See Supplemental Material at http://link.aps.org/supplemental/10.1103/PhysRevResearch.4.023063 for tables of our identified line-graph materials.

[55] B. Sutherland, Localization of electronic wave functions due to local topology, Phys. Rev. B **34**, 5208 (1986).

[56] H. Aoki, M. Ando, and H. Matsumura, Hofstadter butterflies for flat bands, Phys. Rev. B **54**, R17296 (1996).

[57] D. L. Bergman, C. Wu, and L. Balents, Band touching from real-space topology in frustrated hopping models, Phys. Rev. B **78**, 125104 (2008).

[58] H. Tasaki, From Nagaoka's ferromagnetism to flat-band ferromagnetism and beyond an introduction to ferromagnetism in the Hubbard model, Prog. Theor. Phys. **99**, 489 (1998).

[59] A. Tanaka, An Extension of the Cell-Construction Method for the Flat-Band Ferromagnetism, J. Stat. Phys. **181**, 897 (2020).

[60] T. Mizoguchi, M. Maruyama, S. Okada, and Y. Hatsugai, Flat bands and higher-order topology in polymerized triptycene: Tight-binding analysis on decorated star lattices, Phys. Rev. Mater. **3**, 114201 (2019).

[61] J. M. Lee, C. Geng, J. W. Park, M. Oshikawa, S.-S. Lee, H.W. Yeom, and G. Y. Cho, Stable Flatbands, Topology, and Superconductivity of Magic Honeycomb Networks, Phys. Rev. Lett. **124**, 137002 (2020).

[62] L. Elcoro, B. J. Wieder, Z. Song, Y. Xu, B. Bradlyn, and B. A. Bernevig, Magnetic topological quantum chemistry, Nature Commun. **12**, 5965 (2021).

[63] L. W. Beineke, Characterizations of derived graphs, J. Combinatorial Theory **9**, 129 (1970).

[64] W. Setyawan and S. Curtarolo, High-throughput electronic band structure calculations: Challenges and tools, Comput. Mater. Sci. **49**, 299 (2010).

[65] S. P. Ong, W. D. Richards, A. Jain, G. Hautier, M. Kocher, S. Cholia, D. Gunter, V. L. Chevrier, K. A. Persson, and G. Ceder, Python Materials Genomics (pymatgen): A robust, open-source python library for materials analysis, Comput. Mater. Sci. **68**, 314 (2013).

[66] A. Togo and I. Tanaka, Spglib: a software library for crystal symmetry search, arXiv:1808.01590v1.

[67] H. Pan, A. M. Ganose, M. Horton, M. Aykol, K. A. Persson, N. E. R. Zimmermann, and A. Jain, Benchmarking coordination number prediction algorithms on inorganic crystal structures, Inorg. Chem. **60**, 1590 (2021).